Monthly Notices of the ROYAL ASTRONOMICAL SOCIETY

MNRAS **453,** 1396–1403 (2015) doi:10.1093/mnras/stv1728

AMI Galactic Plane Survey at 16 GHz – II. Full data release with extended coverage and improved processing

Yvette C. Perrott,[1⋆] Anna M. M. Scaife,[2] David A. Green,[1] Keith J. B. Grainge,[2] Natasha Hurley-Walker,[3] Terry Z. Jin,[1] Clare Rumsey[1] and David J. Titterington[1]

[1]*Astrophysics Group, Cavendish Laboratory, 19 J. J. Thomson Avenue, Cambridge CB3 0HE, UK*
[2]*Jodrell Bank Centre for Astrophysics, Alan Turing Building, School of Physics and Astronomy, University of Manchester, Oxford Road, Manchester M13 9PL, UK*
[3]*International Centre for Radio Astronomy Research, Curtin Institute of Radio Astronomy, 1 Turner Avenue, Technology Park, Bentley, WA 6845, Australia*

Accepted 2015 July 27. Received 2015 June 19

ABSTRACT

The Arcminute Microkelvin Imager Galactic Plane Survey provides mJy-sensitivity, arcminute-resolution interferometric images of the northern Galactic plane at ≈16 GHz. The first data release covered $76^\circ \lessapprox \ell \lessapprox 170^\circ$ between latitudes of $|b| \lessapprox 5^\circ$; here we present a second data release, extending the coverage to $53^\circ \lessapprox \ell \lessapprox 193^\circ$ and including high-latitude extensions to cover the Taurus and California giant molecular cloud regions, and the recently discovered large supernova remnant G159.6+7.3. The total coverage is now 1777 deg^2 and the catalogue contains 6509 sources. We also describe the improvements to the data processing pipeline which improves the positional and flux density accuracies of the survey.

Key words: catalogues – surveys – ISM: general – Galaxy: general – radio continuum: general.

1 INTRODUCTION

In a previous paper, Perrott et al. (2013, hereafter Paper I), we presented the first data release (DR-I) of the Arcminute Microkelvin Imager Galactic Plane Survey (AMIGPS), a drift scan survey at frequency ≈16 GHz. This provided the most sensitive centimetre-wave Galactic plane survey of large extent at $\nu > 1.4$ GHz, covering 868 deg^2 of the northern Galactic plane at ≈3 arcmin resolution and having noise levels of ≈3 mJy beam^{-1} away from bright sources. The AMIGPS provides a new opportunity to characterize the high-frequency emission of Galactic sources, in particular to identify and investigate the properties of sources which are brighter at 16 GHz than at the lower frequencies (e.g. 1.4 GHz) more often used for Galactic plane surveys. These include dense plasmas, such as compact H II regions, and the anomalous microwave emission first identified by CMB experiments (Leitch et al. 1997) and now demonstrated to exist in many Galactic objects (e.g. Tibbs et al. 2011; Planck Collaboration XV 2014).

The second release (DR-II) of the AMIGPS both extends the coverage of the survey and is produced using an improved data processing pipeline. Here, we briefly describe the improvements to the pipeline and present the new data products.

⋆E-mail: ycp21@mrao.cam.ac.uk

2 OBSERVATIONS

The AMIGPS is observed with the AMI Small Array (SA), a radio interferometer located near Cambridge, UK. It consists of ten 3.7 m diameter dishes, with baselines ranging between 5 and 20 m. It operates between ≈12 and 18 GHz, with the passband divided into eight channels of 0.72 GHz bandwidth; the bottom two are discarded due to a combination of low response and the presence of geostationary satellites. The primary beam at the central frequency of ≈16 GHz is ≈20 arcmin full width at half-maximum (FWHM), and the synthesized beam, which is a measure of the resolution, is ≈3 arcmin FWHM. The telescope is sensitive to angular scales of up to ≈10 arcmin. For further details, see Zwart et al. (2008).

The survey is carried out in drift scan mode, meaning that the telescope is pointed at a fixed hour angle and elevation and observes the sky that drifts past. In practice, the telescope is driven slightly to maintain a fixed J2000 declination, to enable the reobservation of declination strips when necessary. Declination strips are observed at 12 arcmin separation to produce a relatively even noise level across the survey; the theoretical noise varies by ≈3 per cent between the centre of a declination strip and the point halfway between two strips. Dates of the observations range from 2010 June to 2014 October; no attempt to account for source variability is made when mapping.

The coverage of the survey is shown in Fig. 1. The second data release covers $53^\circ \lessapprox \ell \lessapprox 193^\circ$, plus high-latitude extensions to cover the Taurus molecular cloud, the California Giant Molecular Cloud (Lada, Lombardi & Alves 2009), and the newly discovered large

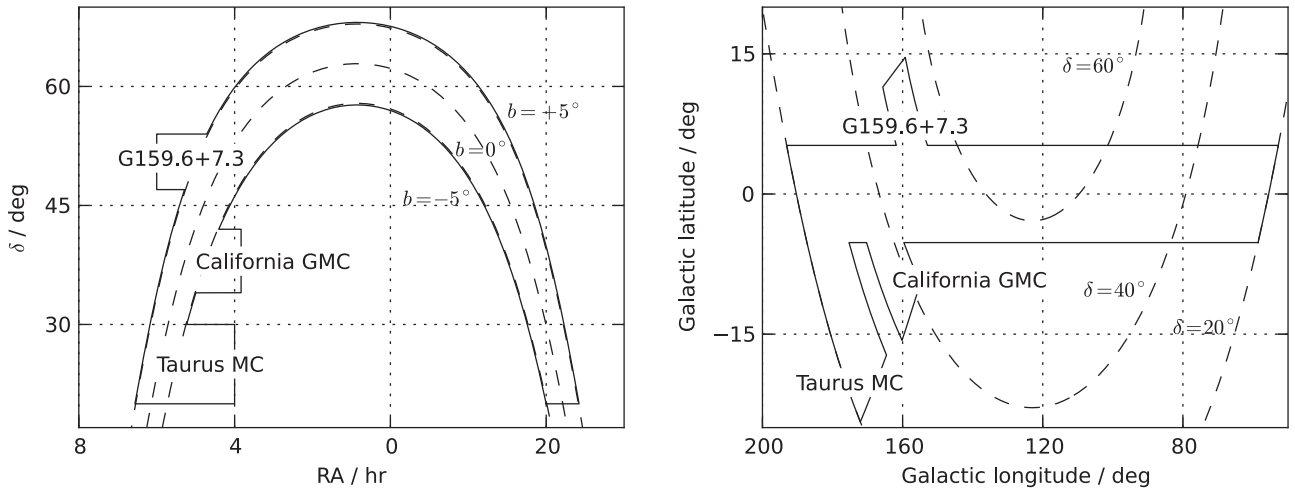

Figure 1. Coverage of the second release of the AMIGPS, in equatorial (left) and Galactic (right) coordinates.

supernova remnant G159.6+7.3 (Fesen & Milisavljevic 2010), for a total of 1777 deg^2.

3 DATA REDUCTION AND MAPPING

Here we briefly outline the data reduction pipeline; for more details see Paper I. The drift scan data were processed using REDUCE, an in-house software tool, to flag shadowing, hardware errors and interference, apply phase and amplitude calibrations, and Fourier transform the lag correlator data to synthesize the frequency channels. Flux density calibration was tied to 3C 286, based on the Perley & Butler (2013) flux density scale. Discrete pointing centres were defined along each declination strip, and the drift scan data points were associated with and phase rotated to their nearest pointing centre; the data were then output as a multisource *uv*-FITS file. Data from any reobservations of the same pointing centre were stacked together in *uv*-space. The pointings were imaged separately in AIPS,[1] then corrected for the primary beam attenuation and combined together in a weighted fashion to form a raster map, using another piece of in-house software, PROFILE (Grainge et al. 2002).

Source-finding is carried out at 5σ on the map, as described in Franzen et al. (2011). The AIPS task JMFIT is used to fit a Gaussian model to each source and the deconvolved source size is used to classify each source as point-like or extended, taking into account the signal-to-noise ratio (SNR) of the source. See Paper I for more details.

3.1 Improvements to the pipeline

This section describes differences to the pipeline described in Paper I, introduced to improve the quality of the final maps.

3.1.1 Interference flagging

The interference flagging generally used for AMI data assumes that the amplitude of an astronomical signal is constant across the course of an observation, while any spikes are assumed to be caused by interference and are removed. For drift scan data, this has the unfortunate effect of also removing the peaks of bright sources visible in the timestream data above the noise level; to stop this from occurring, 'exclusion zones' were defined in the data where the bright sources are present, and those parts of the timestream were not flagged for interference. Previously, these exclusion zones were determined iteratively from the *uv*-data, by searching for peaks above the noise level of the data combined over all baselines; however, this process occasionally misidentified patches of higher noise and interference as sources. The exclusion zones are now redefined from the first-pass maps, by searching for sources of peak flux density $\geq$100 mJy plus adding some regions of high-surface-brightness extended emission manually, and the pipeline is rerun with the improved exclusion zones. In addition, a Kolmogorov–Smirnov (KS) test is run on the phase of the data outside the exclusion zones to identify and remove periods of coherent phase caused by interference. This removes low-amplitude interference that causes striping in the final maps but is not removed by the amplitude interference flagging, present especially at low declination where interference from geostationary satellites is more prevalent. A small amount of manual interference flagging was also performed to remove remaining stripes visible in the maps.

Table 1. Relative weights applied to the survey data, to ensure a consistent central frequency of 15.72 GHz while preserving as far as possible the natural weighting scheme based on the noise properties of the data.

Channel	3	4	5	6	7	8
Weight	0.0908	0.223	0.204	0.200	0.182	0.0997

3.1.2 Frequency correction

Since the raster maps are channel-averaged, differences in flagging can introduce variations in the effective central frequency from pointing to pointing. This is generally a small difference but, particularly at lower declinations where monochromatic interference is often present in the 14.6 GHz channel, can introduce an error in the flux density of up to $\approx$5 per cent for a steep-spectrum ($\alpha = 2$, where $S \propto \nu^{-\alpha}$) source. To correct for this, we reweighted the channel data for each pointing centre so that the relative weights for each channel are as given in Table 1, giving a constant mean frequency of 15.72 GHz. These weights were chosen to represent the natural

[1] Astronomical Image Processing System – www.aips.nrao.edu/

relative weighting of the channels based on the noise properties of the data, for survey data taken between $40^\circ \leq \delta \leq 45^\circ$ which is relatively clean of interference.

3.1.3 Mapping

The previous CLEANing process (see Paper I for details) was found to be over-CLEANing in regions around some bright sources, and was modified as follows. Each pointing was first CLEANed to the first negative component, then the thermal noise σ on the map was estimated using the AIPS task IMEAN. If the brightest pixel was $>5\sigma$, a circular CLEAN box with radius $\approx$1.3 $\times$ the half width at half-maximum (HWHM) of the synthesized beam was placed around the pixel, and the pointing was CLEANed down to 3σ, then the box was removed. The pointing was then CLEANed down to 3σ with no boxes. If the brightest pixel was $\leq 5\sigma$, the pointing was CLEANed down to 3σ with no boxes. In addition, for easier interpretation of the final, combined raster maps, the restoring beam was set as a circular Gaussian with FWHM of 3 arcmin for all pointings.

3.1.4 Beam correction

The primary beam for the drift scan data is the weighted average of the primary beams of each of the samples which have been phase rotated to a given pointing centre; it is elongated along the RA axis compared to the standard SA primary beam. See Paper I for more detail. In the previous pipeline, the CLEANed pointing maps output from AIPS were multiplied by the inverse of the weighted average primary beam; however, for a source visible in a pointing away from the centre, this had the effect of skewing the restoring Gaussian and shifting its centroid by a small but significant amount. In the new pipeline, we instead correct the CLEAN components for the weighted average primary beam and then convolve the corrected CLEAN components with the restoring Gaussian, and add the (beam-corrected) residuals to produce the final pointing map.

We have also improved the description of the primary beam since, from inspection of flux densities of bright, point-like sources appearing at various places in individual pointing centre maps, the Gaussian approximation generally used for the AMI primary beam was found to underestimate the beam correction towards the edges of the maps. When flux densities were measured from the final, combined maps, this caused a small ($\approx$1–2 per cent) underestimation. To improve the characterization of the beam towards the edges, we used sets of drift scans around the bright, point-like radio galaxy 4C 39.25 to fit for the parameters in the (more flexible) AIPS parametrization,

$$\begin{aligned}\text{Primary beam} = {} & 1 + x \times \boldsymbol{pbparm(3)}/10^3 + x^2 \times \boldsymbol{pbparm(4)}/10^7 \\ & + x^3 \times \boldsymbol{pbparm(5)}/10^{10} + x^4 \times \boldsymbol{pbparm(6)}/10^{13} \\ & + x^5 \times \boldsymbol{pbparm(7)}/10^{16},\end{aligned} \tag{1}$$

where $\boldsymbol{pbparm(i)}$ are fitting parameters and $x =$ (distance from the pointing centre in arcmin $\times$ frequency in GHz)^2. There is significant degeneracy between the $\boldsymbol{pbparm(i)}$ parameters, so we constrained each one to lie on a straight line as a function of frequency in Hz, i.e. $\boldsymbol{pbparm(i)} = m_i \times (\nu - \nu_0) + \boldsymbol{pbparm(i)}_0$, where ν_0 is set to 15.75 GHz. Allowing $\boldsymbol{pbparm(7)}$ to vary did not result in a significant improvement in the fit, so we fix it to 0. The best-fitting parameters are shown in Table 2.

The resulting improvement to the agreement with the data, and a comparison between the two beam parameterizations are shown in Fig. 2. Note that in the data reduction pipeline the weighted, average primary beam is cut off at the 10 per cent power point.

Table 2. Fitted parameters for the AIPS parametrization of the SA primary beam as a function of frequency, i.e. $\boldsymbol{pbparm(i)} = m_i \times (\nu - \nu_0) + \boldsymbol{pbparm(i)}_0$ where ν_0 is set to 15.75 GHz.

i	$\boldsymbol{pbparm(i)}_0$	m_i
3	$-2.761\,02 \times 10^{-2}$	$4.504\,61 \times 10^{-13}$
4	$3.248\,52 \times 10^{-3}$	$-1.797\,11 \times 10^{-14}$
5	$-1.899\,70 \times 10^{-5}$	$-2.400\,98 \times 10^{-16}$
6	$4.219\,23 \times 10^{-8}$	$-2.774\,53 \times 10^{-19}$
7	0.000 00	0.000 00

3.1.5 Combining maps

Before combining the individual maps into the large raster maps, the individual maps are regridded to the raster map grid using the AIPS task REGRD, to take advantage of this more sophisticated regridding algorithm compared to the simple algorithm used for the task previously in PROFILE. This has the effect of increasing source flux densities measured from the combined maps by a mean of $\approx$1 per cent.

4 COMPARISON TO DR-I

To investigate the differences between DR-I and DR-II, we matched sources within 1 arcmin ($\approx 2\sigma$ for the lowest SNR of 5 for the larger beam size of 3 arcmin used in DR-II) in the two catalogues. This produced 3157 matches, i.e. 90 per cent of the sources in DR-I have matches in DR-II. The 346 sources without matches in the DR-II catalogue are either low-SNR and have dropped below the 5σ threshold due to repositioning of noise spikes, are on or near patches of extended emission and have had their centroid shifted due to the different imaging procedures, or are near a bright source whose exclusion zone has changed and are now excluded.

2423 of the sources are classified as point-like in both the DR-I and DR-II catalogues. The peak flux densities and SNRs for these sources are compared in Fig. 3. It can be seen that flux densities are generally slightly higher in DR-II; this is due to the improved primary beam correction as explained in Section 3.1.4. Also, SNRs for low-to-medium-SNR sources are increased slightly due to the improvements in interference flagging; SNRs for high-SNR sources are decreased due to the improvement in the CLEANing algorithm which no longer artificially decreases the noise around bright sources. Comparisons for extended sources are more complicated and are not attempted here.

5 CALIBRATION ACCURACY OF DR-II

5.1 Positional accuracy

Similarly to Paper I, the errors $\sigma_{\rm RA}$ and σ_δ in RA and δ for a point source are assumed to be given by

$$\sigma^2_{\rm RA\ or\ \delta} = \epsilon^2_{\rm RA\ or\ \delta} + \frac{\theta^2}{2\ln(2)\,{\rm SNR}^2}, \tag{2}$$

where $\epsilon_{\rm RA\ or\ \delta}$ are the rms calibration errors in RA and δ and the second term is the noise-like uncertainty in each direction (now the

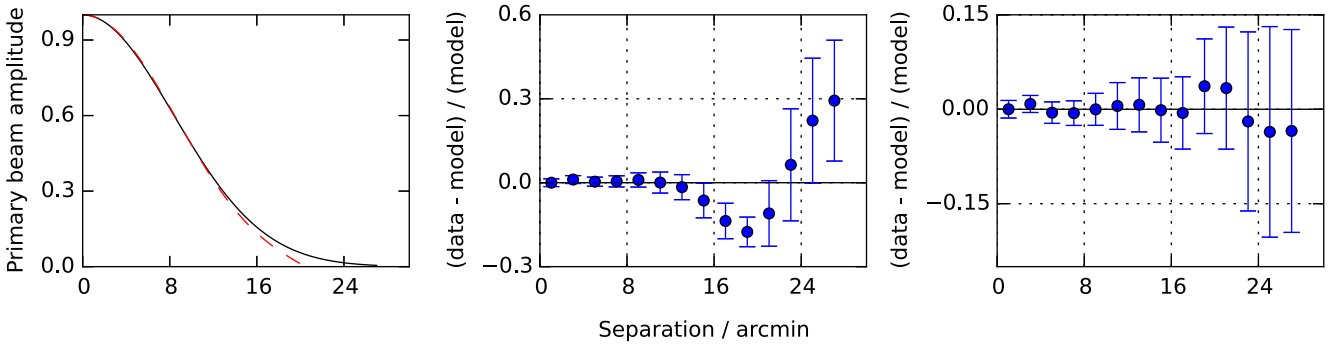

Figure 2. The left-hand plot shows the standard Gaussian primary beam model (black, solid line), and new, fitted AIPS parametrization (red, dashed line), for the central frequency. The two right-hand plots show fractional residuals with respect to the Gaussian primary beam model (centre), and new, fitted AIPS parametrization (right) at the central frequency, for a set of channel-averaged drift scans around 4C 39.25. The data are averaged in bins of 2 arcmin in separation from the source, and the error bars show the standard deviation within each bin. Note the difference in *y*-axis scale. In the AMIGPS data reduction pipeline, the weighted, average primary beam is cut off at the 10 per cent power point.

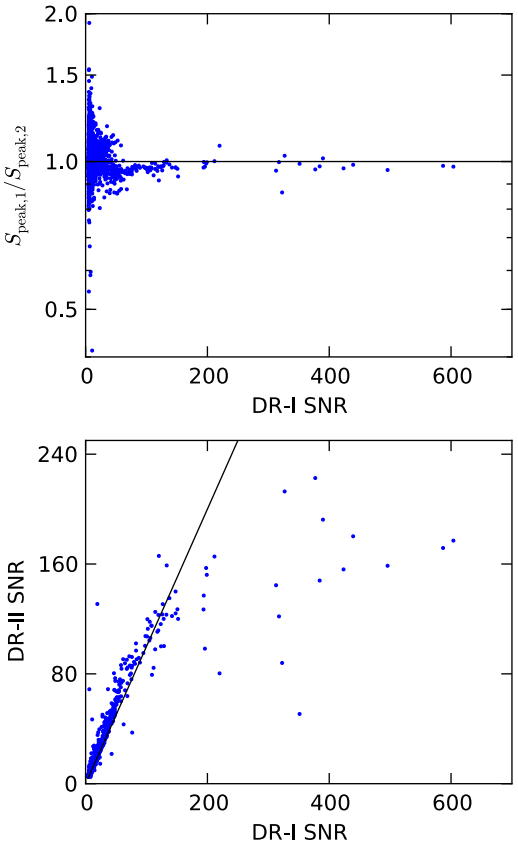

Figure 3. Comparison between peak flux densities (top) and SNRs (bottom) for sources classified as point-like in both DR-I and DR-II. The black line shows the one-to-one correspondence in both cases. The improvements in the pipeline have produced a slight increase in flux density in DR-II compared to DR-I. For low-to-medium-SNR sources, the SNR is increased slightly, while for high-SNR sources it is decreased.

same in both directions since the beam is round); θ is the FWHM of the synthesized beam, always 180 arcsec in DR-II.

For DR-II, we found $\epsilon_{\rm RA} = 1.6$ arcsec and $\epsilon_{\delta} = 1.9$ arcsec by minimizing the KS statistic for the separations between the detected and true (to milliarcsec accuracy) positions of 252 Very Long Baseline Array Calibrator Survey (VCS; Beasley et al. 2002) catalogue sources (cf. 2.6 and 1.7 arcsec, respectively, in DR-I). The two calibration error terms are now very similar, indicating that the systematic effect introduced by primary-beam-correcting the restoring Gaussian (see Section 3.1.4), which was worse in the RA direction due to the beam elongation, has been eliminated by the improved pipeline.

As in DR-I, the positional uncertainties for extended sources are calculated as

$$\sigma^2_{\rm RA\ or\ \delta} = \epsilon^2_{\rm RA\ or\ \delta} + \sigma^2_{\rm J,RA\ or\ J,\delta}, \quad (3)$$

where the appropriate $\sigma_{\rm J}$ terms are the errors estimated by the AIPS fitting task JMFIT, which folds in an estimate of the noise-like error as well as the error associated with the fit.

5.2 Flux density accuracy

As in DR-I, we assume flux calibration errors are given by

$$\sigma^2_S = (0.05\,S)^2 + \sigma^2, \quad (4)$$

where S is peak (integrated) flux density for a point-like (extended) source. This error estimation comprises a 5 per cent calibration uncertainty and a noise-like error σ which for a point-like source is the rms map noise measured from the CLEANed map, and for an extended source is the error estimated by JMFIT which also folds in an estimation of the fitting error. Note that this does not account for the effect of flux loss for extended sources.

We tested the flux density calibration accuracy by searching for semiconcurrent pointed observations of VCS sources, which are used as phase calibrators for AMI observations and so are observed on a regular basis. We remapped individual drift scan observations containing these sources using the standard pipeline and compared the source flux density measured from the drift scan map to the mean of any pointed observation flux density measurements taken within 10 d (to limit variability), for 111 drift scan/pointed observation matches. Fig. 4 shows the ratio of drift scan to pointed observation flux density as a function of the distance of the source from the centre of the declination strip; the worst outliers lie at the edge of the strip, where direction-dependent effects (which can suppress flux) are expected to be worst.

96 per cent of the drift scan flux densities lie within 3σ of the pointed observation flux density (cf. 93 per cent for DR-I). Excluding the 3σ outliers and taking the median percentage difference shows that the drift scan flux densities are biased low by $\approx$1 per cent (cf. 2 per cent for DR-I); this is a common effect in surveys (see e.g.

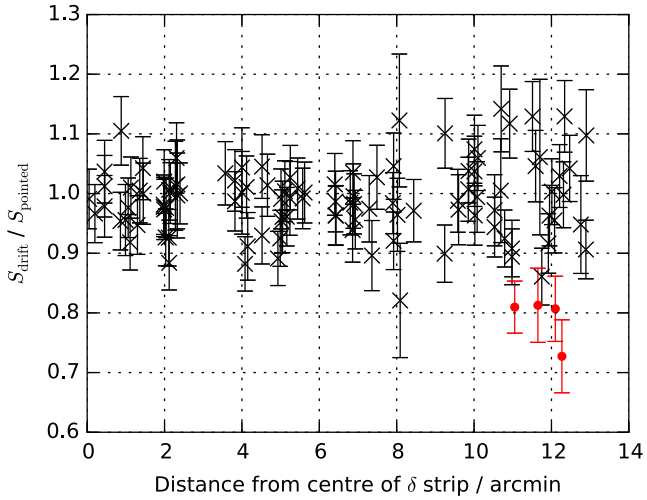

Figure 4. Ratios of flux densities measured from drift scan observations and mean of pointed observations taken within 10 d, as a function of the position of the source with respect to the centre of the drift scan observation. The error bar shows the drift scan error only. Black crosses (red dots) show points at $\leq (>) 3\sigma$.

Davies et al. 2011) and we do not correct for this small error. This bias is fairly insensitive to the number of days within which the match is performed, and the exclusion of points at greater distance from the centre of the strip.

6 COMPLETENESS

Estimation of the completeness of the survey, or the fraction of sources expected to be detected over the survey region at a given flux density level, is made difficult due to the 'exclusion zones' which were employed around bright sources to account for elevated, non-Gaussian noise present around sources with peak flux density $\gtrsim$ 50 mJy (see Paper I). Sources within the 'exclusion radius' of a bright source with peak flux density $S_{\rm peak,\,bright}$ were required to have peak flux density $S_{\rm peak} \geq S_{\rm peak,\,bright}/10$ to be included in the catalogue, effectively redefining the noise level within the exclusion zone to be $\max(\sigma_{\rm orig}, S_{\rm peak,\,bright}/50)$ where $\sigma_{\rm orig}$ is the existing thermal noise estimate from the map.

The probability of a source with true flux density $\hat{S}$ being detected when lying on a pixel with thermal noise $\sigma_{\rm n}$ is given by

$$P(\hat{S} \geq 5\sigma_{\rm n}) = \int_{5\sigma_{\rm n}}^{\infty} \frac{1}{\sqrt{2\pi\sigma_{\rm n}^2}} \exp\left(-\frac{\left(x-\hat{S}\right)^2}{2\sigma_{\rm n}^2}\right) {\rm d}x, \qquad (5)$$

assuming Gaussian statistics. The theoretical probability of the source being detected can therefore be calculated by averaging the probabilities given by equation (5) for each pixel in the map. This is illustrated in Fig. 5 and was calculated by (a) using pixels outside the exclusion zones only (dashed line) and (b) using all pixels in the map, and assuming that the effective noise level defined above for the pixels inside exclusion zones can be treated as an approximation to the Gaussian noise level $\sigma_{\rm n}$ in equation (5) (solid line).

The accuracy of these completeness curves was also tested via simulation. Simulated sources at a given flux density were inserted in the maps using the AIPS task IMMOD at random positions; the standard source-finding pipeline was run on the maps and the fraction of sources detected was recorded for each peak flux density. The results of the simulations agreed very well with the theoretical curves in Fig. 5.

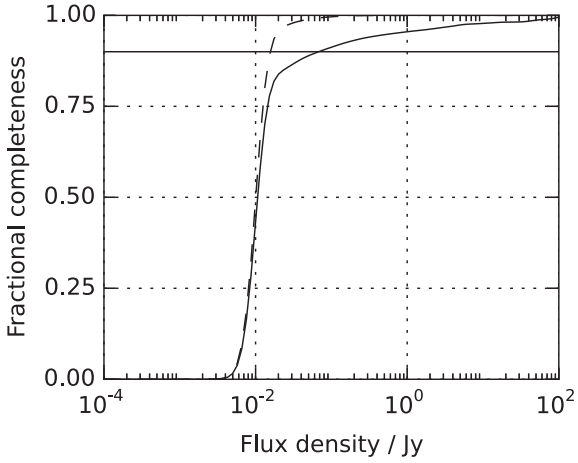

Figure 5. An estimation of the completeness of the AMIGPS DR-II calculated from the noise maps. The completeness was calculated over the whole survey area (solid line) and outside the exclusion zones around bright sources only (dashed line). The horizontal line shows the 90 per cent completeness limit.

Outside the exclusion zones, the survey is 90 per cent complete above ≈16 mJy, but when including the exclusion zones it does not reach 90 per cent completeness until ≈68 mJy. It should be noted however that any effect due to correlation between source positions is not included in the completeness estimation. The completeness curve for the whole survey is expected to be slightly overestimated due to this effect.

7 DATA PRODUCTS

The maps and full source catalogue are now available online at http://www.astro.phy.cam.ac.uk/surveys/amigps and from CDS (http://cdsarc.u-strasbg.fr/viz-bin/qcat?J/MNRAS/). Maps are presented in Galactic coordinates covering the main survey area and the extensions separately. Each map also has an associated noise map and 'adjusted' noise map which shows the effective noise level after adjusting for bright sources (see Paper I for more details). We show two example maps in Section 8.

The catalogue contains a total of 6509 sources. As in DR-I, for each source the catalogue contains the following.

(i) A source name, constructed from the J2000 RA and δ coordinates of the source.

(ii) The peak RA ($\rm RA_{peak}$), δ ($\delta_{\rm peak}$), flux density ($S_{\rm peak}$) and associated errors ($\Delta\rm RA_{peak}$, $\Delta\delta_{\rm peak}$, $\Delta S_{\rm peak}$); these are the appropriate quantities to use for point-like sources.

(iii) The fitted centroid RA ($\rm RA_{cent}$) and δ ($\delta_{\rm cent}$), integrated flux density ($S_{\rm int}$) and associated errors ($\Delta\rm RA_{cent}$, $\Delta\delta_{\rm cent}$, $\Delta S_{\rm int}$); these are the appropriate quantities to use for extended sources.

(iv) The critical source size ($e_{\rm crit}$, size below which a source is classified as point-like; see Paper I) and the deconvolved source major and minor axis sizes and position angle ($e_{\rm maj}$, $e_{\rm min}$, e_θ). A deconvolved size of 0.0 indicates that the source was not found to be wider than the synthesized beam in the major or minor axis direction.

(v) The χ^2 value for the fit (note that this is an indication of the goodness of fit of the Gaussian model to the source, not of the reliability of detection of the source).

(vi) The source classification (point-like or extended).

A sample section of the catalogue is shown in Table 3.

Table 3. An example catalogue showing the parameters of the brightest 20 sources detected in Fig. 6. See Section 7 for a description of the quantities. Coordinates are J2000, coordinate errors are in arcsec, flux densities are in mJy, and angular sizes are in arcsec. Galactic coordinates (in degrees) are also added for ease of comparison with Fig. 6; these are not in the AMIGPS catalogue.

Source	RA_{peak}	δ_{peak}	ΔRA_{peak}	$\Delta\delta_{peak}$	ℓ_{peak}	b_{peak}	S_{peak}	ΔS_{peak}	RA_{cent}	δ_{cent}	ΔRA_{cent}	$\Delta\delta_{cent}$	S_{int}	ΔS_{int}	e_{crit}	e_{maj}	e_{min}	e_θ	χ^2	Type
AMIGPS J210937+501334	21:09:37.21	+50:13:34.1	2.6	2.8	91.12	1.58	1073.9	55.7	21:09:36.40	+50:13:36.6	2.0	2.2	1425.2	77.4	100.0	114.9	81.7	106.6	2.91	E
AMIGPS J212044+515324	21:20:44.85	+51:53:24.3	2.2	2.5	93.53	1.47	901.6	46.0	21:20:44.62	+51:53:23.4	1.8	2.1	857.3	45.5	100.0	16.2	0.0	21.2	1.59	P
AMIGPS J211229+523240	21:12:29.71	+52:32:40.0	6.4	6.5	93.12	2.84	630.9	40.7	–	–	–	–	–	–	109.1	–	–	–	–	–
AMIGPS J210920+522333	21:09:20.90	+52:23:33.1	3.5	3.6	92.68	3.08	458.4	24.7	21:09:21.85	+52:23:40.9	2.4	2.6	616.5	36.4	100.0	142.8	70.9	48.0	5.08	E
AMIGPS J212437+505842	21:24:37.19	+50:58:42.8	2.9	3.1	93.32	0.4	317.4	16.6	21:24:35.76	+50:59:01.8	2.6	2.5	619.9	33.8	100.0	328.3	0.0	129.8	12.60	E
AMIGPS J210515+493959	21:05:15.32	+49:39:59.7	3.3	3.5	90.23	1.72	309.2	16.5	21:05:15.70	+49:40:12.3	2.3	2.5	398.6	23.2	100.0	112.5	71.8	131.0	4.01	E
AMIGPS J210618+475108	21:06:18.59	+47:51:08.2	2.4	2.6	89.0	0.38	233.6	12.0	21:06:19.13	+47:51:09.3	1.8	2.1	226.0	12.2	100.0	0.0	0.0	0.0	3.36	P
AMIGPS J211351+522729	21:13:51.78	+52:27:29.9	10.0	10.0	93.2	2.63	218.7	17.8	21:13:49.23	+52:27:54.6	5.8	5.6	319.2	33.9	136.9	140.9	82.1	127.0	1.59	E
AMIGPS J211215+522451	21:12:15.05	+52:24:51.0	18.7	18.7	93.0	2.77	212.6	28.0	–	–	–	–	–	–	188.3	–	–	–	–	–
AMIGPS J210217+470217	21:02:17.46	+47:02:17.9	2.6	2.8	87.94	0.34	207.5	10.7	21:02:17.13	+47:02:18.5	1.9	2.1	195.1	10.8	100.0	0.0	0.0	0.0	1.30	P
AMIGPS J211221+521947	21:12:21.95	+52:19:47.1	16.9	16.9	92.95	2.7	193.1	23.3	–	–	–	–	–	–	179.1	–	–	–	–	–
AMIGPS J211415+495345	21:14:15.31	+49:53:45.2	3.5	3.6	91.39	0.81	154.9	8.4	21:14:15.17	+49:53:45.3	2.2	2.5	152.3	9.3	100.0	29.3	0.0	5.4	1.40	P
AMIGPS J210821+493644	21:08:21.89	+49:36:44.2	4.1	4.2	90.53	1.31	111.8	6.2	21:08:21.83	+49:36:42.4	2.4	2.6	104.5	6.9	100.0	0.0	0.0	0.0	1.56	P
AMIGPS J211852+493700	21:18:52.75	+49:37:00.2	3.6	3.7	91.71	0.08	107.1	5.8	21:18:52.73	+49:36:55.2	2.2	2.4	93.6	5.9	100.0	0.0	0.0	0.0	2.13	P
AMIGPS J210056+533133	21:00:56.25	+53:31:33.0	4.7	4.8	92.68	4.78	96.1	5.6	21:00:56.17	+53:31:34.6	2.6	2.8	83.5	6.0	100.0	0.0	0.0	0.0	1.50	P
AMIGPS J210344+495157	21:03:44.32	+49:51:57.9	5.2	5.3	90.22	2.04	87.3	5.2	21:03:44.24	+49:51:58.8	2.9	3.1	87.5	6.5	100.0	51.9	0.0	42.4	0.88	P
AMIGPS J210538+480716	21:05:38.23	+48:07:16.9	4.1	4.2	89.13	0.64	85.9	4.8	21:05:37.94	+48:07:13.8	2.4	2.6	77.8	5.2	100.0	0.0	0.0	0.0	1.73	P
AMIGPS J205642+494004	20:56:42.45	+49:40:04.3	4.8	5.0	89.32	2.76	74.9	4.4	20:56:42.21	+49:40:00.6	2.7	2.9	70.0	5.1	100.0	52.8	0.0	47.8	1.22	P
AMIGPS J204207+500351	20:42:07.24	+50:03:51.9	6.1	6.2	88.14	4.84	71.5	4.5	20:42:07.65	+50:03:53.6	3.1	3.4	63.0	5.4	106.4	0.0	0.0	0.0	2.55	P
AMIGPS J211331+503908	21:13:31.59	+50:39:08.1	4.8	4.9	91.86	1.42	71.0	4.1	21:13:31.36	+50:39:08.6	2.5	2.8	60.2	4.4	100.0	0.0	0.0	0.0	1.06	P

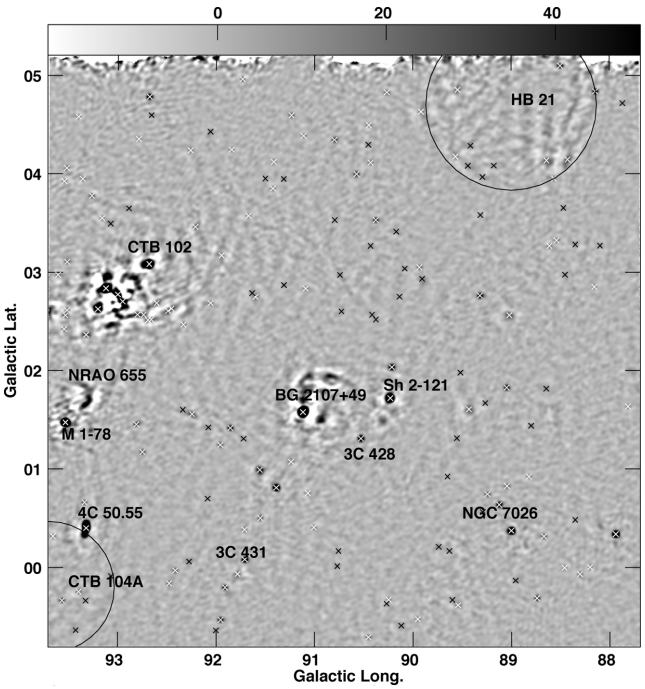

Figure 6. One of the AMIGPS 6° × 6° square raster maps covering the main survey area. The grey-scale is in mJy beam^{-1} and has been truncated at −20 and +50 to show low-surface-brightness features. Detected sources are marked with ×, and several known objects are marked (see text for details). The large circles mark the approximate outlines of the supernova remnants HB 21 and CTB 104A. The resolution of the map is 3 arcmin.

8 EXAMPLE MAPS AND CATALOGUE

8.1 G90.70+2.20

Fig. 6 shows one of the 6° square raster maps covering the main survey area, centred at $\ell = 90.^\circ7$, $b = +2.^\circ20$. There are 160 sources detected in this map, of which 120 are classed as point-like, 32 as extended, and 8 as undefined (the Gaussian fit failed in these cases). For comparison in Fig. 7 we show the (total-power) Canadian Galactic Plane Survey (CGPS; Taylor et al. 2003) map at 1.4 GHz covering the same region. As an example of the AMIGPS catalogue format we show the catalogue entries for the brightest 20 sources in this field in Table 3. For ease of comparison with Fig. 6 we also give Galactic coordinates in Table 3; these are not included in the AMIGPS catalogue.

The AMI map shows features covering a range of angular scales, from the very large, such as the supernova remnants HB 21 (Hanbury Brown & Hazard 1953) and CTB 104A (Wilson 1963) and the H II region complexes CTB 102 (Wilson & Bolton 1960), BG 2107+49 (Higgs & Vallee 1984), and NRAO 655 (Pauliny-Toth, Wade & Heeschen 1966), to the medium, such as the H II region Sh 2-121 (Sharpless 1959) which is extended slightly to the AMIGPS beam, to the point-like, such as the planetary nebula NGC 7026 (Dreyer 1888) and the compact H II region M 1–78 (Minkowski 1946). Some extragalactic sources are also visible, including 3C 428, 3C 431 (Edge et al. 1959) and 4C 50.55 (Pilkington & Scott 1965). From comparison to the CGPS map it is clear that only the sharp knots and filaments in the extended structures are visible, and the smooth, large-scale emission is resolved out.

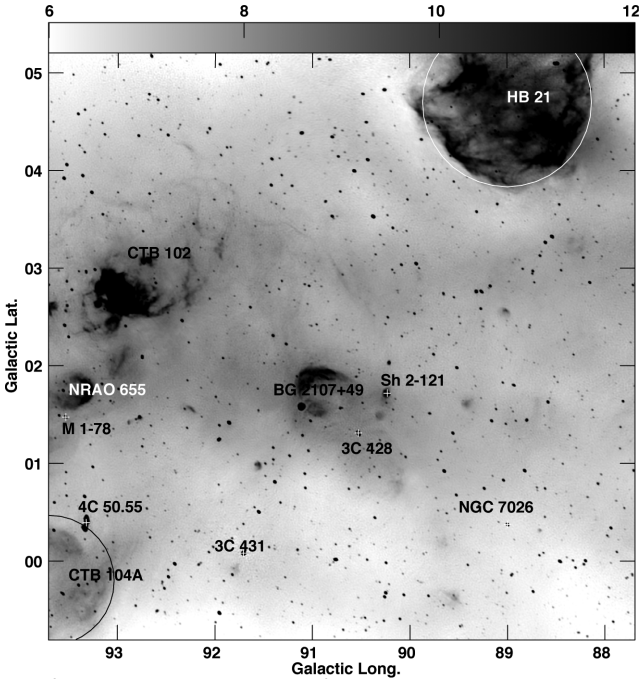

Figure 7. The same area as Fig. 6, as seen in the CGPS. The grey-scale shows brightness temperature in K and has been truncated at 6 and 12 to show low-surface-brightness features. Several known objects are marked (see text for details). The large circles mark the approximate outlines of the supernova remnants HB 21 and CTB 104A. The resolution of the map is ≈1.3 arcmin.

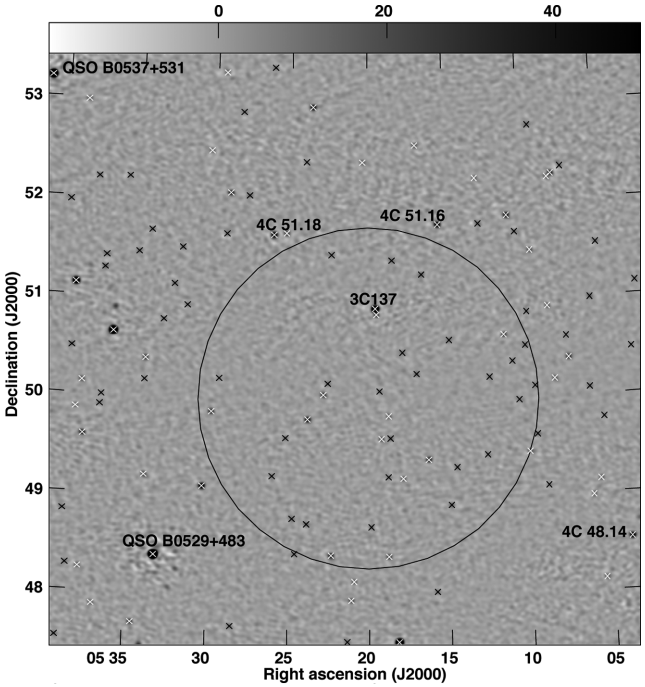

Figure 8. A 6° × 6° region of the extension covering the supernova remnant G159.6+7.3. The grey-scale is in mJy beam^{-1} and has been truncated at −20 and +50 to show low-surface-brightness features. Detected sources are marked with ×, and six of the brightest, known sources are labelled; they are all extragalactic. All of the sources in this field are compact and are likely to be extragalactic. The large circle marks the approximate outline of the supernova remnant, which is not detected. The resolution of the map is 3 arcmin.

8.2 G159.6+7.3

As an example of a section of the survey containing mostly (if not all) extragalactic sources, in Fig. 8 we show a 6° × 6° region of the extension covering the supernova remnant G159.6+7.3. 116 sources are detected in this field, all of which are compact. This is a large (≈3° × 4°), faint remnant discovered in H α in the Virginia Tech Spectral Line Survey (Fesen & Milisavljevic 2010). Although the supernova remnant is large in extent, it has sharp, filamentary structures at the rim which should be minimally affected by flux loss in the AMI map (see their figs 3 and 4). No emission is visible in the AMI map; the maximum noise inside the annulus containing the H α emission is 3.2 mJy beam^{-1} (the mean is 1.7 mJy beam^{-1}) so we estimate a conservative 5σ upper limit on the filamentary emission at 15.72 GHz of 16 mJy beam^{-1}. Assuming a typical spectral index of $\alpha = 0.5$, where $S \propto \nu^{-\alpha}$, this corresponds to a surface brightness limit of ≈10^{-21} W m^{-1} Hz sr^{-1} at 1 GHz, with the caveat that smooth, extended emission will be resolved out. A more detailed comparison would take into account the AMIGPS *uv*-sampling; this is available on request from the authors.

9 CONCLUSIONS

We present the second data release of the AMI Galactic Plane Survey, covering the northern Galactic plane at $\delta \gtrapprox 20°$ between $b \approx \pm 5°$, corresponding to $53° \lessapprox \ell \lessapprox 193°$, plus high-latitude extensions to cover the Taurus and California giant molecular cloud regions and the supernova remnant G159.6+7.3. This extends the coverage of the survey from 868 deg^2 in the first data release to 1777 deg^2. The resolution of the survey is 3 arcmin and the noise level is ≈3 mJy beam^{-1} away from bright sources. This is the most sensitive and highest resolution large-area Galactic plane survey at cm-wave frequencies above 1.4 GHz.

The pipeline used to produce the survey maps has been improved with respect to that used for DR-I, producing small improvements in positional accuracy (rms calibration errors are now 1.6 and 1.9 arcsec in RA and δ, respectively) and flux calibration accuracy (flux densities of sources near the edge of strips are less likely to be biased downwards). The maps and catalogue of 6509 sources are available online from CDS (http://cdsarc.u-strasbg.fr/viz-bin/qcat?J/MNRAS/) and http://www.astro.phy.cam.ac.uk/surveys/amigps.

ACKNOWLEDGEMENTS

We thank the staff of the Mullard Radio Astronomy Observatory for their invaluable assistance in the commissioning and operation of AMI, which is supported by Cambridge University and the Science and Technologies Facilities Council. This work has made use of the distributed computation grid of the University of Cambridge (CAMGRID). This research has made use of NASA's Astrophysics Data System Bibliographic Services and the facilities of the Canadian Astronomy Data Centre operated by the National Research Council of Canada with the support of the Canadian Space Agency. The research presented in this paper has used data from the CGPS, a Canadian project with international partners supported by the Natural Sciences and Engineering Research Council. YCP acknowledges support from a CCT/Cavendish Laboratory studentship and a Trinity College Junior Research Fellowship. CR and TZJ

acknowledge support from Science and Technology Facilities Council studentships.

REFERENCES

Beasley A. J., Gordon D., Peck A. B., Petrov L., MacMillan D. S., Fomalont E. B., Ma C., 2002, ApJS, 141, 13
Davies M. L. et al., 2011, MNRAS, 415, 2708
Dreyer J. L. E., 1888, Mem. R. Astron. Soc., 49, 1
Edge D. O., Shakeshaft J. R., McAdam W. B., Baldwin J. E., Archer S., 1959, Mem. R. Astron. Soc., 68, 37
Fesen R. A., Milisavljevic D., 2010, AJ, 140, 1163
Franzen T. M. O. et al., 2011, MNRAS, 415, 2699
Grainge K., Jones M. E., Pooley G., Saunders R., Edge A., Grainger W. F., Kneissl R., 2002, MNRAS, 333, 318
Hanbury Brown R., Hazard C., 1953, MNRAS, 113, 123
Higgs L. A., Vallee J. P., 1984, J. R. Astron. Soc. Can., 78, 155
Lada C. J., Lombardi M., Alves J. F., 2009, ApJ, 703, 52
Leitch E. M., Readhead A. C. S., Pearson T. J., Myers S. T., 1997, ApJ, 486, L23
Minkowski R., 1946, PASP, 58, 305
Pauliny-Toth I. I. K., Wade C. M., Heeschen D. S., 1966, ApJS, 13, 65
Perley R. A., Butler B. J., 2013, ApJS, 204, 19
Perrott Y. C. et al., 2013, MNRAS, 429, 3330 (Paper I)
Pilkington J. D. H., Scott J. F., 1965, Mem. R. Astron. Soc., 69, 183
Planck Collaboration XV, 2014, A&A, 565, A103
Sharpless S., 1959, ApJS, 4, 257
Taylor A. R. et al., 2003, AJ, 125, 3145
Tibbs C. T. et al., 2011, MNRAS, 418, 1889
Wilson R. W., 1963, AJ, 68, 181
Wilson R. W., Bolton J. G., 1960, PASP, 72, 331
Zwart J. T. L. et al., 2008, MNRAS, 391, 1545

SUPPORTING INFORMATION

Additional Supporting Information may be found in the online version of this article:

DR2_cat.dat (http://mnras.oxfordjournals.org/lookup/suppl/doi:10.1093/mnras/stv1728/-/DC1).

Please note: Oxford University Press are not responsible for the content or functionality of any supporting materials supplied by the authors. Any queries (other than missing material) should be directed to the corresponding author for the article.

This paper has been typeset from a TEX/LATEX file prepared by the author.